Additive Manufacturing 36 (2020) 101536

Contents lists available at ScienceDirect

Additive Manufacturing

journal homepage: www.elsevier.com/locate/addma

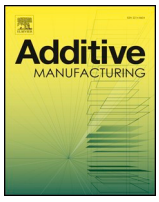

# Crack initiation and growth in additively printed ABS: Effect of print architecture studied using DIC

John P. Isaac, Sivareddy Dondeti, Hareesh V. Tippur*

*Department of Mechanical Engineering, Auburn University, AL, 36849, United States*

ARTICLE INFO

*Keywords:*
Fused filament fabrication
Print architecture
Fracture mechanics
Crack growth resistance
Digital image correlation

ABSTRACT

Acrylonitrile Butadiene Styrene or ABS is a popular and inexpensive isotropic, amorphous thermoplastic widely used for Additive Manufacturing (AM) of engineering parts. An AM process called Fused Filament Fabrication (FFF) involving layer-by-layer deposition of melted thermoplastic wire through a heated nozzle along predetermined paths is common for printing thermoplastics such as ABS. Individual layers printed during AM can be configured differently and could introduce anisotropy into the part due to weaker planes between individual beads even when the feedstock is isotropic. This research examines the tensile and fracture behaviors of three in-plane print architectures, namely $[0^\circ/90^\circ]_n$, $[45^\circ/-45^\circ]_n$ and $[0^\circ/45^\circ/90^\circ/-45^\circ]_n$ orientations. The full-field measurement of local in-plane displacements are performed optically using Digital Image Correlation (DIC) method up to crack initiation and during crack growth in quasi-statically loaded 3-point bend edge-notched specimens. A simple method of analyzing DIC data by transferring it to a corresponding finite element model for computing the *J*-integral and then partitioning it into individual stress intensity factors is developed. Even though the printed architectures show macroscopic elastic isotropy, significant differences in the failure strain, crack initiation and growth parameters, and failure modes among the three architectures are observed. These differences are explained using tests performed on comparable unidirectional prints. The results suggest that $[0^\circ/45^\circ/90^\circ/-45^\circ]_n$ are preferable to the other two more common configurations for a relatively graceful failure behavior and higher resistance to crack growth, suggesting that better fracture performance could be achieved by manipulating print architecture.

## 1. Introduction

Additive Manufacturing (AM) has become a popular production process for building 3D objects layer-by-layer [1]. Different materials such as plastics, metals, ceramics, are currently being manufactured through AM. Because of its capability to produce parts with complex geometries on demand and/or in limited quantities, AM has been growing rapidly over the past decade or so and has found numerous automotive, aerospace, medical applications. Fused Filament Fabrication (FFF) (also called Fused Deposition Modeling or FDM) is one of the various types of AM processes used extensively to print thermoplastics [2]. In FFF, thermoplastics available as filament/wire stock are melted and deposited via heated nozzles layer-by-layer on a heated bed in predetermined computer-generated deposition paths [3]. Due to low melting point, thermoplastics such as PLA, ABS, PET, PA, PVA are some of the polymers commonly printed using FFF. However, the printing process introduces artifacts in the printed parts which affect their mechanical failure characteristics and hence needs to be investigated when parts are to meet critical functionality. In addition to this, the option of prescribing the print path of the nozzle potentially introduces anisotropy in terms of weak planes in AM parts [4]. Hence the role of print architecture on general mechanical failure and fracture properties needs to be studied carefully [5].

One of the popular amorphous thermoplastics used for in FFF or FDM is Acrylonitrile Butadiene Styrene or ABS [6]. Various other thermoplastics, possessing different characteristics such as bio-compatibility and/or compliancy, are also used in disparate, sometimes unconventional applications such as dental and medical field (implants, prosthetics), furniture and fashion industry (shoes, watches), aviation and automotive field (fuel injection nozzle) [7,8]. Hence it is important to understand the effects of the printing parameters and architectures before employing ABS parts produced by AM for everyday use. The effects of build direction and raster orientation on mechanical failure were studied in [9] by performing tension tests. The differences between the prints were explained using fractographic analyses to emphasize the significance of print architecture on mechanical strength.

* Corresponding author.
*E-mail address:* htippur@eng.auburn.edu (H.V. Tippur).

https://doi.org/10.1016/j.addma.2020.101536
Received 9 April 2020; Received in revised form 27 June 2020; Accepted 8 August 2020
Available online 27 August 2020
2214-8604/ © 2020 Elsevier B.V. All rights reserved.

The size dependent anisotropy in terms of flexural moduli and strain distributions in two unidirectionally printed ABS beams measured using DIC were reported in [10]. Some studies have focused on enhancing the fracture properties of printed parts by predefining nozzle paths based on the knowledge of stresses acting on the parts [11]. The fracture toughness was found to increase in additively printed ABS samples under mixed-mode loading when the deposition path was guided by the principal stress directions [12]. Some studies have also shown that infill pattern and the build direction with respect to the pre-crack affects the failure parameters [13–16]. Currently, the woven multi-laminate composites are being additively manufactured and this has resulted in increased shear strength [17]. With ABS as the copolymer and thermoplastic polyurethane (TPU) as an additive, a polymer matrix was manufactured using FFF process and was found to have enhanced adhesive properties [18]. In terms of fracture properties, layer orientation, build orientation and infill percentages were found to be the main factors controlling the fracture toughness of AM parts produced through FFF process [19–22]. Since polymer-based AM parts are used extensively in day-to-day applications [23] with potential of AM to produce critical load bearing parts, it is important to study the differences in behaviors of these materials because of factors such as the layer architecture in detail. Although some previous works [15,16,19,22] have reported on the fracture behavior in terms of crack initiation, most have relied on far-field load or deflection measurements. Some [10,16] have utilized optical imaging but local measurements have not been incorporated to study the crack growth behavior in detail. Thus, no work has been reported on both the crack initiation and growth behaviors based on local mechanical fields to reveal intricacies of the fracture behavior of 3D printed parts.

In this work, three different planar print architectures, namely $[0^\circ/90^\circ]_n$, $[\pm 45^\circ]_n$ and $[0^\circ/45^\circ/90^\circ/-45^\circ]_n$ are employed to evaluate the tensile and the fracture properties of additively manufactured ABS coupons under quasi-static loading conditions. Digital Image Correlation (DIC), a popular full-field optical metrology commonly used for non-contact, vision-based strain analysis, is used to measure surface deformations [24]. In many previous studies on traditional structural materials, the measured displacements obtained from DIC are used in conjunction with the theoretical expressions and over-deterministic least-squares analyses to determine the crack tip fracture parameters such as Stress Intensity Factors (SIF) [25–27]. In this work, a simple approach of transferring experimentally measured displacements obtained from DIC to customized Finite Element (FE) discretization to (a) extract the energy release rate (the *J*-integral), and (b) compute individual mixed-mode SIFs [28] using proven algorithms available in ABAQUS, ANSYS, etc. A few previous works [29–32] have carried out calculations on traditional materials but by applying measured displacements from optical measurements as boundary conditions for FE sub-models. In this work, however, the geometry of the specimen surface in the Region-of-Interest (ROI) recorded by the camera is modeled as a FE mesh in ABAQUS by matching the DIC grid. The measured displacements are then imported into the discretized model as full-field surface boundary conditions. Subsequently, the in-built modules in ABAQUS are employed for extracting the fracture parameters. The work, on the whole, emphasizes print architecture induced complexities of fracture and failure mechanics of AM parts as well as its potential for enhancing the overall mechanical performance.

**Table 1**
3D printer parameters.

| Print parameters | Values | Print parameters | Values |
|---|---|---|---|
| Extruder temperature | 240 °C | Layer thickness | 0.2 mm |
| Bed temperature | 115 °C | Wall thickness | 0.8 mm |
| Chamber temperature | 50 °C | Infill speed | 80 mm/s |
| Nozzle flow % | 100 % | Nozzle retraction speed | 40 mm/s |

In the following, details about specimen fabrication followed by information regarding different print architectures studied are described first. The description of tension, ultrasonic and quasi-static fracture experiments is provided in the subsequent sections. Then, a detailed explanation of the methodology of extracting relevant fracture parameters is included before presenting the results pertaining to the role of print architecture on crack initiation and growth responses. It is followed by a discussion of results before presenting major conclusions of the work.

## 2. Specimen fabrication

A Cubicon 3DP-110 F printer was used to print all specimens studied in this work. The desired geometry was modeled using Solidworks® and exported to a slicer software as a stereolithographic (.STL) file. All print settings and modifications were finalized using the slicer software and a G-code was generated and exported to the printer. Planar architectures namely, $[0^\circ]_n$, $[90^\circ]_n$, $[0^\circ/90^\circ]_n$, $[45^\circ/-45^\circ]_n$ and $[0^\circ/45^\circ/90^\circ/-45^\circ]_n$ were printed[1] with identical printer parameters listed in Table 1. The $[0^\circ]_n$, $[90^\circ]_n$ architectures were used as *reference* architectures to explain the mechanical responses observed in mixed-direction builds namely $[0^\circ/90^\circ]_n$, $[45^\circ/-45^\circ]_n$ and $[0^\circ/45^\circ/90^\circ/-45^\circ]_n$. A 100 % infill option was selected for all architectures to obtain fully dense specimens and to avoid effects of any additional porosity other than the one inherent to the printing process itself.

During printing, the outer wall was deposited first in each layer of the specimen and then the printer nozzle was moved in directions specific to the above patterns in the *x*–*y* plane. A schematic of the layer buildup (in the *z*-direction) used for the three architectures are shown in Fig. 1. For the two reference architectures namely $[0^\circ]_n$, $[90^\circ]_n$, deposition in the *x*–*y* plane were all either parallel or perpendicular to the *x*-direction within the outer wall and simply repeated in the *z*-direction until the desired thickness was reached. Within each layer, the nozzle followed a serpentine path. In the mixed-direction prints such as in $[0^\circ/90^\circ]_n$, a repeating two layer buildup was adopted. That is, the printer nozzle was moved parallel to the *x*-axis for the first layer and perpendicular to the *x*-axis in the second layer, and so on. This was repeated in the *z*-direction. Similarly, in the $[45^\circ/-45^\circ]_n$ architecture, the first layer was at 45° to the *x*-axis and the second layer was at -45° to the *x*-axis. In the $[0^\circ/45^\circ/90^\circ/-45^\circ]_n$ architecture, on the other hand, a repeating four layer buildup of a combination of the two preceding architectures was implemented. That is, the first layer was along 0°, the second was along 45°, the third was along 90° and the fourth was along -45° to the *x*-axis. The subsequent layers were repeated thereafter. *Henceforth, for simplicity of description,* $[0^\circ/90^\circ]_n$, $[45^\circ/-45^\circ]_n$ *and* $[0^\circ/45^\circ/90^\circ/-45^\circ]_n$ *architectures will be identified as* A1, A2 *and* A3*, respectively*. Although ABS is a nominally isotropic material, because of the differences in rastering, anisotropy in terms of weak planes occur in the printed specimens.

## 3. Experimental details

### 3.1. Tension tests on A1, A2, A3 architectures

First, uniaxial tension tests were carried out on all three print architectures A1, A2 and A3, described earlier. An Instron 4465 mechanical tester fitted with a 5 kN load-cell was used to carry out tests on dog-bone shaped specimens of 8 mm width and 4 mm thickness in the gage section. Fig. 2(a) shows the dimensions of the specimen used. They

[1] It should be noted that $[0^o/90^o]_n$ and $[45^o/-45^o]_n$ are default architectures in most 3D printers and the rationale for these architectures from the mechanical performance perspective is mostly intuitive. Therefore, for starters, the $[0^o/45^o/90^o/-45^o]_n$ architecture was chosen besides the $[0^o/90^o]_n$ and $[45^o/-45^o]_n$ to demonstrate that there could be other raster patterns among the infinite number of possibilities for achieving better mechanical performance.

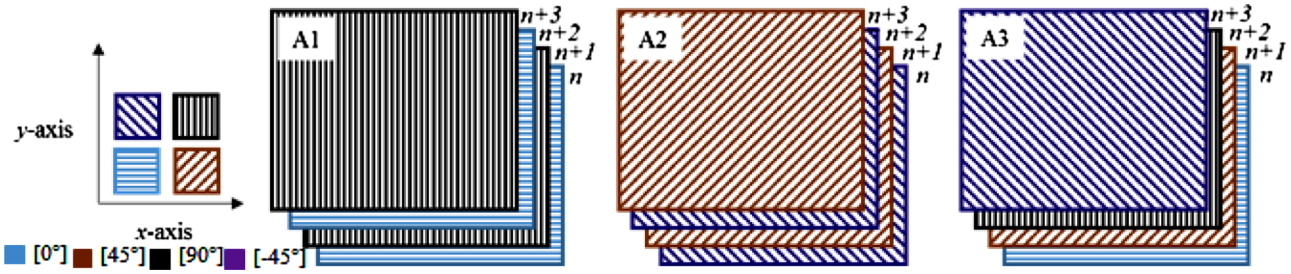


**Fig. 1.** Build direction of each layer of print architectures designated A1, A2 and A3. A serpentine pattern was adopted during printing of each layer of the architecture. *The hatch marks in each layer correspond to* 0°, 45°, 90°, -45° *directions.*

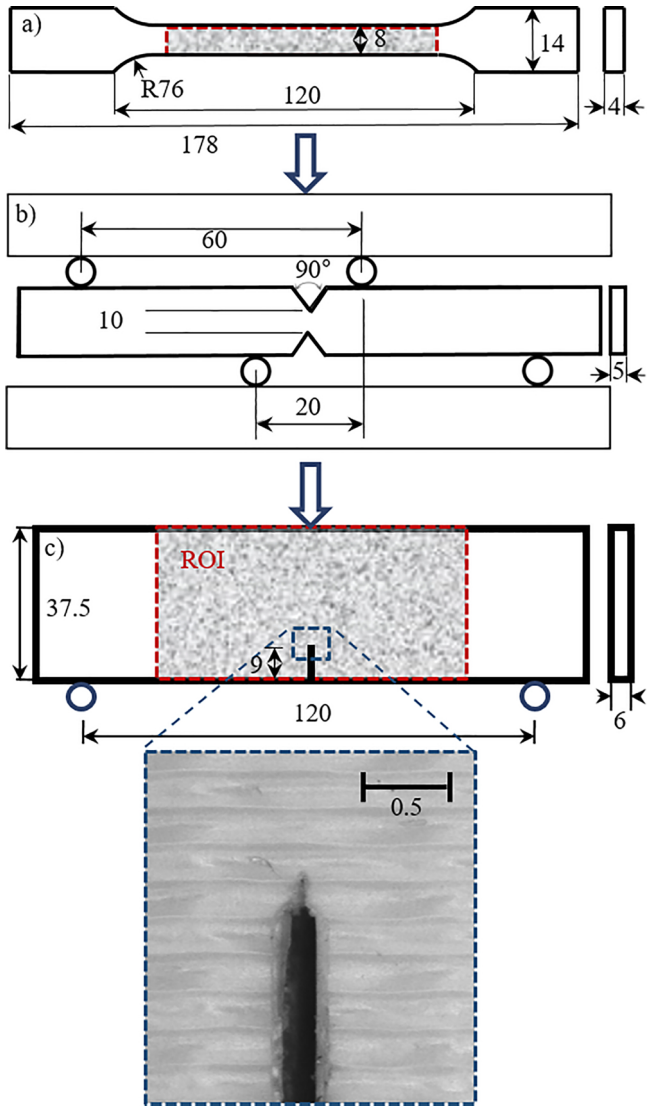


**Fig. 2.** **(a)** Tension specimen geometry. **(b)** Iosipescu shear tests specimen geometry and loading configuration. **(c)** Quasi-static fracture specimen loading and geometry with an inset of the crack tip sharpened by a razor blade. (*All dimensions are in mm*).

were sprayed with fine mists of black and white paint to create random speckles on one of the surfaces to perform 2D-DIC in the gage section and measure in-plane deformations. A PointGrey camera (2048 × 2048 pixels fitted with an 18−108 mm focal length macro zoom lens) recorded the event at a rate of 2 frames per second (fps). The experiments were performed in displacement control mode at a crosshead speed of 0.05 mm/s. During each test, time, load and crosshead displacement data were all recorded until the specimen failed.

### 3.2. Tension and shear tests on reference architectures

Uniaxial tension and pure shear tests were carried out next on the reference architectures with $[0^\circ]_n$ and $[90^\circ]_n$ raster. This included (a) separate uniaxial tension tests on plain $[0^\circ]_n$ and $[90^\circ]_n$ architectures, and (b) Iosipescu shear tests [33] on $[0^\circ]_n$ samples (Fig. 2(b)). As noted earlier, in these reference architectures, all the layers over the entire build thickness in the $z$-direction of the sample were unidirectional but other specimen details were same as the ones used for A1, A2 and A3.

### 3.3. Ultrasonic tests

Ultrasonic measurements were made on 12.7 mm cubes printed in A1, A2 and A3 architectures. An ultrasonic tester, Olympus Epoch 600, was used for launching elastic waves into the specimen in all three directions and in all three print architectures. The elastic wave speeds for both longitudinal and shear waves were recorded along all three axes of rotation. A schematic of the setup used in these measurements is shown in Fig. 3. Longitudinal (2.25 MHz) ($C_L$) and shear (5 MHz) ($C_S$) wave transducers were employed separately to measure the time-of-flight using which the respective wave speeds were determined. These values and mass density (ρ) (measured separately) were then used in conjunction with Eq. (1) to calculate the *dynamic* elastic constants, $E$ and $\nu$.

$$C_L = \sqrt{\frac{E(1-\nu)}{\rho(1+\nu)(1-2\nu)}},\ C_S = \sqrt{\frac{E}{2\rho(1+\nu)}} \tag{1}$$

### 3.4. Fracture tests

Next, fracture tests were carried out under quasi-static loading conditions on all three print architectures - A1, A2 and A3. Fig. 2(c) shows dimensions of edge-notched symmetric three-point bend specimens. A 6 mm long notch was inserted into the specimen edge using a 0.3 mm thick circular saw at the mid-span and its root was sharpened by scoring the notch-front with a razor blade to achieve a sharp starter

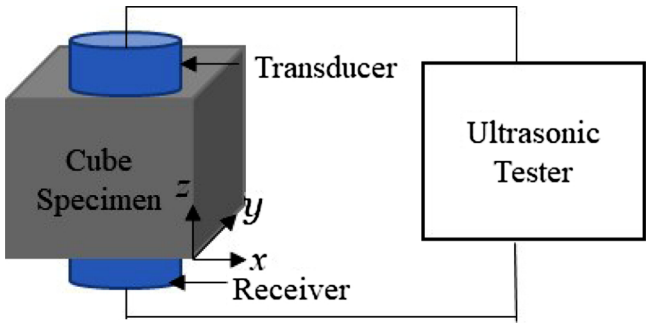


**Fig. 3.** Ultrasonic test setup.

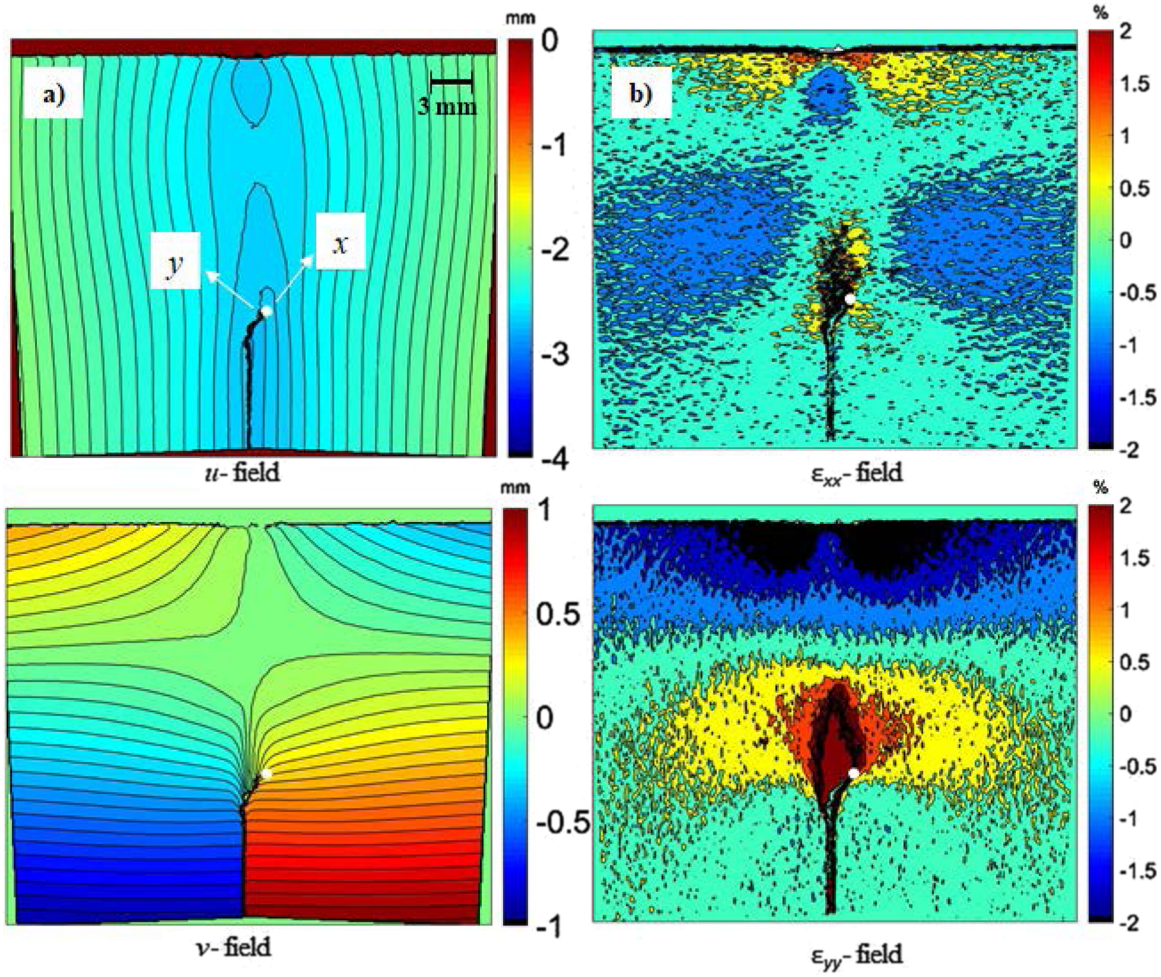


**Fig. 4.** Two orthogonal displacement fields, $u$ and $v$ in the $x$ and $y$-directions **(a)** and the corresponding normal strain fields **(b)** from DIC at a time instant/load step (load = 1082 N). A higher noise level in the strain field relative to the displacement fields is evident. (The displacement contour increment in (a) is 50 μm.).

crack (Fig. 2(c)). Again, an Instron 4465 mechanical tester with a 5 kN load cell, equipped with a roller loading pin of diameter 0.5 inch, was used to carry out these experiments at a crosshead speed of 0.007 mm/s and time, load, and crosshead displacement data were all recorded during each test. As in the tension tests, a fine coat of random speckles was sprayed on one of the surfaces of the specimen in order to perform DIC and quantify in-plane displacements. Again, the PointGrey camera was used to record the speckle images at 2 fps during tests. As in the tension tests, specimens of all three architectures were tested until crack initiation and significant growth occurred. Other experimental parameters related to DIC can be found in the Appendix A, Table A1.

### 3.5. Extraction of fracture parameters

The 2D-DIC method was used to measure two orthogonal in-plane displacement components on the specimen surface in the vicinity of the growing crack [26,27,34]. The displacements can be numerically differentiated to find the strain fields and other deformation gradients. The numerically obtained derivatives from DIC are often noisy, particularly when deformations are small. (Fig. 4 shows experimentally measured displacement and resulting normal strain fields from DIC for a typical experiment on ABS, to be discussed subsequently.) Hence, the deformation gradients needed to calculate fracture parameters namely the path independent $J$-integral [35,36],

$$J = \lim_{\Gamma \to 0} \int_{\Gamma} (W\delta_{1i} - \sigma_{ij}\frac{\partial u_j}{\partial x_1})n_i \; dC, \quad (i, j = 1, 2; x_1 = x, x_2 = y), \tag{2}$$

using the standard *line integration* approach is challenging. In the above, $W$ is the strain energy density ($=\frac{1}{2}\sigma_{ij}\varepsilon_{ij}$), $\sigma_{ij}$ and $u_j$ are the Cartesian components of the stress ($\sigma_{11} = \sigma_{xx}$, $\sigma_{12} = \sigma_{xy}$, etc.) and displacements ($u_1 = u$, $u_2 = v$), $n_i$ are components of the unit vector normal to the counterclockwise contour path $\Gamma$, $\delta_{1i}$ is the Kronecker delta and $dC$ is the arc length along the contour. Being a path independent quantity, the $J$-integral is often evaluated as a line integral. But it can also be expressed as area or surface integrals.

As noted in the literature review, the measured displacement fields can be analyzed directly by using them in conjunction with the prevailing elastic crack tip fields and over-deterministic least-squares analyses approaches [27,34,37,38]. Thus measured fracture parameters are generally sensitive to the number of terms of the asymptotic displacement field employed, the rigid body motions/rotations suffered by the specimen during loading, domain over which the data is extracted, out-of-plane displacements due to crack tip triaxiality, etc. The results often are sensitive to the location of the crack tip in the speckle image and/or the displacement field. Moreover, the $J$-integral method does not depend on fitting a field description to obtain the fracture properties. In light of these, a simpler method of transferring the two measured orthogonal displacement data arrays from DIC into a 2D finite element model as surface (boundary) input to compute the energy release rate using robust *domain* (*area*) *integral* algorithms by defining the $J$-integral as,

$$J = \int_{A} \left(-W\delta_{1i} + \sigma_{ij}\frac{\partial u_j}{\partial x_1}\right)\frac{\partial q_1}{\partial x_1} dA, \; (i, j = 1, 2) \tag{3}$$

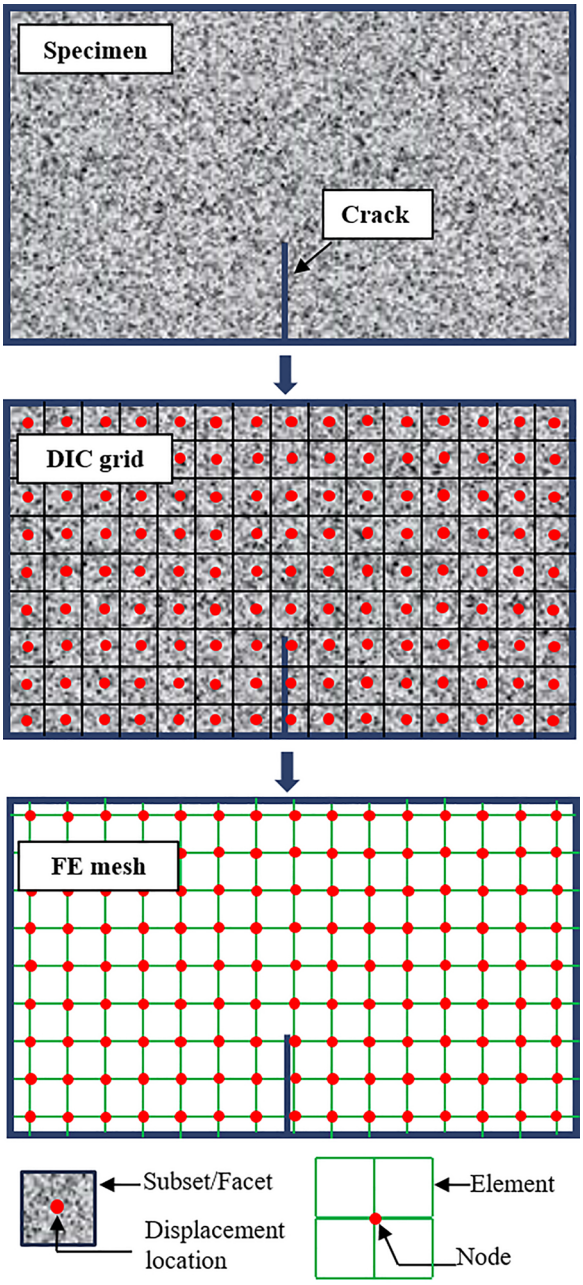


**Fig. 5.** The approach to compute the *J*-integral and SIFs by transferring DIC data into FE discretization for domain integration and mode-partitioning. The red dots are center of sub-image and nodes of the FE grid. (For interpretation of the references to colour in this figure legend, the reader is referred to the web version of this article).

is more attractive. In the above equation, $A$ is the area of the domain/ribbon of elements encircling the crack tip, $q_1$ is a sufficiently smooth weighting function, and all others parameters are as defined previously. Furthermore, this approach allows decomposition of the computed *J*-integral subsequently into individual stress intensity factors ($K_I$ and $K_{II}$ in this work) using mode-partitioning based assumed pure auxiliary fields [39,40] and invoking small scale yielding. This allows additional insight into the failure modes at play in the 3D printed architectures. Accordingly, this new approach was adopted in this work.

In DIC, the recorded images in the reference and deformed states are segmented into subsets/sub-images of gray scales. Subsequently, the displaced location of a subset in the deformed state is determined relative to its undeformed state using a gray scale correlation algorithm.

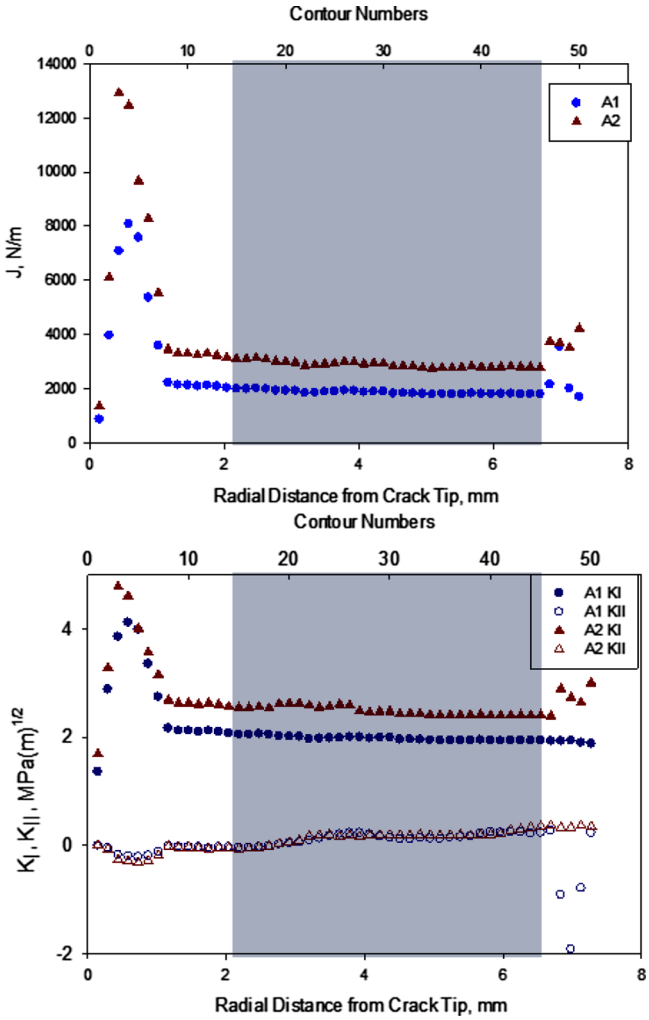


**Fig. 6.** Plots of $J$, $K_I$ and $K_{II}$ for different contour number. Contour #15-45 corresponding to approx. 2.25-7 mm or $r/B$ ratio of 0.4-1.2 are used consistently for all load steps. (The reported data corresponds to the shaded part where the $J$-value varies by < 4%).

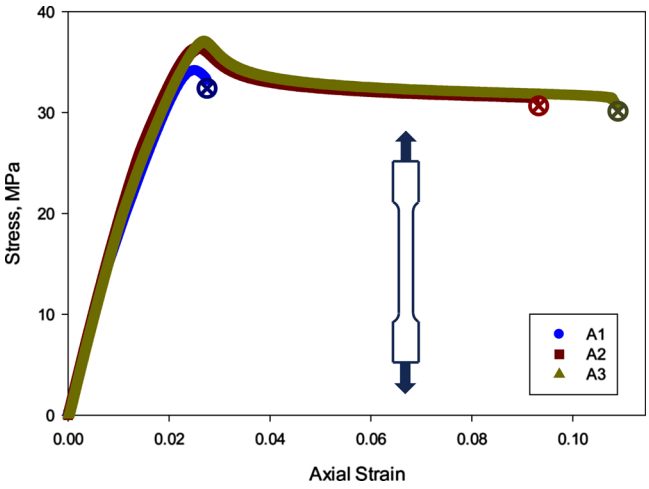


**Fig. 7.** Tensile stress-strain responses of dog-bone specimens of different print architectures. (The cross marks indicate specimen failure).

In doing so, each displacement data point in the full-field is an average value computed over the corresponding subset *at its center*. To implement the proposed approach, careful meshing was carried out in such a

**Table 2**
Material properties obtained from tensile tests.

| Material Property | A1 | A2 | A3 |
|---|---|---|---|
| Elastic modulus (GPa) | 2.07 | 2.14 | 2.14 |
| Poisson's ratio | 0.34 | 0.34 | 0.34 |
| Failure stress (MPa) | 34.1 | 36.3 | 36.8 |
| Failure strain % | 2.8 | 9.3 | 10.9 |

way that these displacement locations match the nodal locations in the finite element model consisting of a square grid of quad elements parallel and perpendicular to the specimen edges. It should be noted, however, that when the crack followed a kinked path[2] relative to its initial orientation, the neighborhood of the crack (region adjacent to the flanks) was discretized along a band using quad elements and the nodes were inputted with *interpolated* displacement boundary conditions from DIC subsets. It should be also noted that the crack tip was modeled simply as a sharp discontinuity since the *measured* displacements were used as 'input' to the FE model to *dictate* post-processing of DIC data to find the *J*-integral and then SIFs. Hence it should be noted that the sharpness of the crack tip in the model is unimportant; it is only the location and the orientation that matters.

A schematic of the steps followed is shown in Fig. 5. Experimentally measured displacement components from DIC were then imported as nodal 'boundary conditions' for the discretized field. The FE model was then run using ABAQUS structural analysis software (v.16.1) after identifying the current crack tip position and its orientation to evaluate the fracture parameters using in-built algorithms. Using the computed *J*-integral, the two stress intensity factors (SIFs) $K_I$ and $K_{II}$ were calculated via the interaction integral method [40] and small scale yielding assumption. (The mathematical details of this method can be found in ABAQUS documentation.)

The fracture parameters are reported by ABAQUS for different contours. The first contour corresponds to the ring of elements encircling and embracing the crack tip and the second includes the first and the second rings, and so on. That is, as the contour number increases, the radial extent of the domain around the crack tip used for computing the *J*-integral increases. Since, the discretization corresponds to the sub-image overlap used while performing DIC (sub-image size = 25 × 25 pixels and step size = 5 pixels, scale factor (optical magnification) ~ 0.030 mm/pixel), each additional ring corresponds to the radial increment equal to the sub-image overlap × the scale factor. Fig. 6 shows two examples of such plots of the *J*-integral and the corresponding $K_I$ and $K_{II}$ values in terms of the contour numbers at crack initiation for the A1 and A2 architectures. Evidently, the values do not show path independence in the very close vicinity of the crack tip (up to contour #7 or ~1 mm) due to a combination of out-of-plane displacements due to triaxial effects, inelastic deformations violating small scale yielding assumptions, and the finite element size and shape functions, among others. However, at larger distances of 2.25 − 7 mm ($r/B$ ratio ~ 0.4–1.2, where $r$ is the radial distance from crack tip and $B$ is the specimen thickness) away from the crack tip, the values are rather stable and nearly constant (with ~4% variation). These stable values, averaged over contours 15–45 or 2.25 mm–7 mm (shaded region in Fig. 6), were recovered as the *J*-integral. Subsequently, fracture modes were partitioned to obtain $K_I$ and $K_{II}$ for that time instant or load step (justification of utilizing small yielding assumption is offered in the 'Results' section). In the FE computations, four node bilinear plane stress quadrilateral element (CPS4R) of size 0.15 mm (scale factor × step size) with two degrees of freedom per node was used. It should be noted that this element shape and size were preferred to match the DIC grid. The potential error in the computed *J*-integral and SIFs due to crack tip location from the speckle images and the displacement contours was examined. The location of the crack tip was found to be within 2 pixels. The resulting variability of the *J*-Integral and SIFs was less than 2%. Additional information in this regard for an example case can be found in Appendix A (see, Fig. A1).

[2] When there was an increase in length or change in direction, FE models were updated with the new crack tip location; the new crack orientation was identified relative to the previous step.

## 4. Results

### 4.1. Tension tests

The tensile stress-strain responses on two sets of specimens of all three architectures were measured. Results for one of the two sets are shown in Fig. 7. *Graphs for each specimen* type initially showed a linear response, up to approx. 1.5 % engineering strain and *overlap on each other. This suggests that despite the differences in print architectures of* A1, A2 *and* A3*, they are all elastically same.* The elastic modulus was measured in each case using linear regression of data up to 0.1 % strain. The spray painted random speckles were recorded to measure longitudinal and lateral strains in the gage section of the specimen using DIC to enable evaluation of the elastic constants $E$ and $\nu$ for each architecture. For brevity, a pair of representative strain fields from a uniaxial test on A1 architecture is shown in Appendix A. The strains from DIC were relatively uniform in the gage section Fig. A2(a). The figure also shows stress vs. axial and transverse strain plots (Fig. A2(b)) in the linear range for this architecture. These tension tests were repeatable for all three architectures. Two test results are shown for each of the architectures in Fig. A3(a) and good repeatability is self-evident.

The elastic modulus ($E$) and the Poisson's ratio ($\nu$) were found to be nearly same for all the three architectures and the difference for $E$ was less than 4%. In addition to the elastic constants, Table 2 lists other parameters from the uniaxial tension experiments. Each of the architectures showed a peak stress followed by a softening response, either with or without a distinct plateau region before an abrupt failure. The A1 architecture was found to have the lowest failure stress, peak/ultimate stress and strain at failure. The A2 architecture had a marginally higher (~7%) peak stress relative to A1 (0°/90° case) whereas there was a substantial increase in the failure strain, by over 230 %. The A3 architecture had a response similar to that of A2 [45/-45° case] in terms of its peak stress. The failure strain, however, was even higher (by ~17 %) relative to the A2 architecture (or, by 290 % relative to A1). The increase in the strain at failure signifies higher ductility observed in the A2 and A3 architectures relative to A1. *More interestingly, the higher ductility of* A3 *relative to* A2 *is unexpected* and needs to be further explored.

To understand these differences in stress vs. strain responses due to print architectures, particularly in the inelastic regime, images of failed cross-sections from tension tests were recorded using a Keyance VHX 6000 digital microscope and are shown in Fig. 8. In the A1 architecture, thinning of individual print layers normal to the loading direction was visible along with evidence of disbonded layers. The A2 architecture shows relatively denser fracture surface with large regions of failure in shear, seen as swaths of featureless zones connected by shear steps, consistent with the higher ductility relative to A1. The A3 architecture shows features in between those of A1 and A2 with partial alignment of the disbonded layers and shear steps with smaller featureless zones. These differences in features are attributed to higher ductility and toughness of A2 and A3 architectures.

### 4.2. Tension and shear tests on reference architectures

The stress-strain responses for the reference architectures are shown in Fig. 9. Fig. 9(a) and (b) shows the tensile stress-strain responses. The results (peak stress ~35 MPa for 0° print and ~40 MPa for the 90° print, strain-at-failure ~2.4 % in both cases) are nearly same as the one for the A1 (Fig. 7) architecture. The pure shear tests (Fig. 9(c)) based on

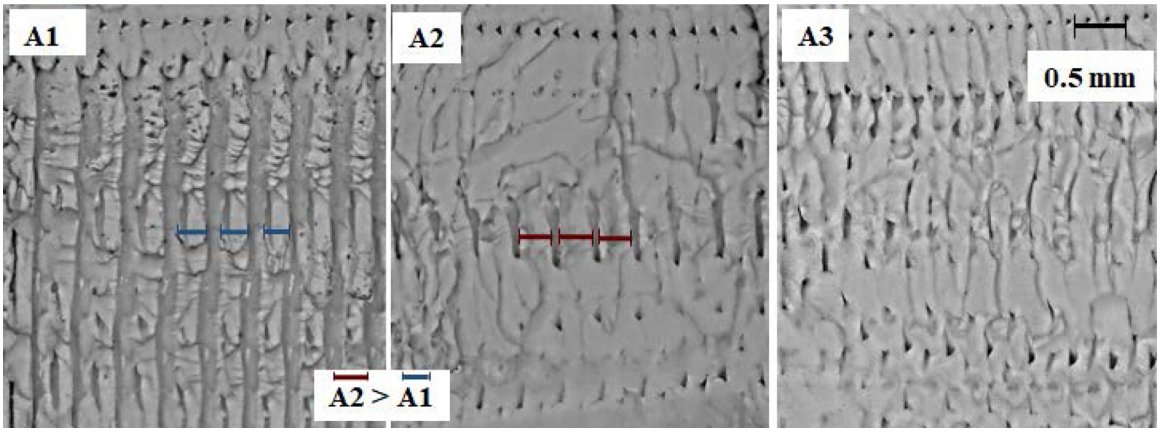


**Fig. 8.** Optical micrographs of fractured cross-section of tensile specimens. (Blue and Red bars highlight the relative thinning of individual print lines in A1 relative to A2.). (For interpretation of the references to colour in this figure legend, the reader is referred to the web version of this article).

Iosipescu geometry, on the other hand, show that the ultimate shear stress is ~35 MPa, close to the tensile strength of the unidirectional coupons. However, the shear strain at failure is ~23 %, *ten times higher than the tensile failure strain of the 0° or 90° prints* (and the A1 architecture).

### 4.3. Ultrasonic results

The fact that the elastic moduli measured from uniaxial tension tests for A1, A2 and A3 and the two reference architectures (Tables 2 and 3) are all nearly identical is interesting and rather unexpected given significant differences in the failure behaviors. Ultrasonic tests were carried out to explore this macroscale *elastic isotropy* further and the resulting measurements are enumerated in Table 4.

Evidently, the values of $E$ are expectedly higher than the ones from uniaxial tests due to the high strain rates (MHz frequency) of the ultrasonic transducer vs. the low strain rates (sub-Hz frequency) used during quasi-static tests. More importantly, the values of these dynamic elastic constants were same in all three directions and for the all three architectures. Thus, the 3D printed architectures were *macroscopically isotropic* despite the differences in the underlying print architectures.

### 4.4. Fracture tests

The load vs. load-point displacement plots for edge-cracked 3-point bend specimens for all three architectures are shown in Fig. 10(a). The response for the A1 architecture shows a relatively brittle response when compared to A2 and A3 counterparts. Following a linear increase up to crack initiation occurring at a peak load, a precipitous drop in load to complete fracture occurred in A1. In the A2 and the A3 architectures, on the other hand, the response was linear up to crack initiation and was significantly higher (~40 %) relative to the A1 architecture. More importantly, a relatively gradual (as opposed to an abrupt) drop in load occurred during crack growth in A2 and A3 architectures. Furthermore, the A3 architecture showed visibly wavy load-deflection response during crack growth relative to A2. To quantify these observations, histograms of energy absorbed (area under the curve) by the three architectures before and after crack initiation were obtained and are shown in Fig. 10(b). The energy absorbed before crack initiation was approx. 130 % higher for the A2 and A3 architectures relative to A1, whereas the energy absorbed during crack propagation was ~800 % higher for the A2 and 1400 % higher for the A3 architecture relative to A1. These are consistent with the higher ductility of A2 and A3 architectures observed relative to A1.

Fig. 11 shows reassembled photographs of the fractured specimens to illustrate crack propagation in all three architectures under quasi-static loading conditions. In the A1 architecture, the crack propagated self-similarly or along the direction of the pre-crack. On the other hand, the crack propagated in a staircase pattern, in one of the two 45° directions, in A2 whereas in A3, the crack growth was locally and incrementally along ± 45° as well as 0° directions with a substantial meandering and frequent jumps in between different layers along the crack path. *The latter is consistent with the wavy load-deflection response seen in* Fig. 10*(a)*. As a result, the overall macroscopic crack growth direction is noticeably different from the ± 45° directions observed in A2. Evidence of crazing, though not readily evident from the photographs due to the white color of ABS material used, was also observed at the crack tip and along the crack flanks indicating significantly higher crack growth resistance in the A2 and A3 architectures relative to A1. The manifestation of shear deformations along the crack path is clearly visible from the noticeable kink in crack surface striations in A3.

The gray scale photographs of surface speckles (Figs. 12(c)–14(c) ) recorded by the camera in the deformed state were correlated with the reference images recorded before the application of load to obtain the displacement component fields in two orthogonal directions, along ($x$) and perpendicular ($y$) to the initial crack orientation. An image analysis software, ARAMIS®, was used to perform gray scale correlation by segmenting images into 25 × 25 pixel sub-images with 5 pixels step size. The scale/magnification factor was ~30 μm/pixel for these images. Figs. 12–14 show representative contours of two select orthogonal displacement components namely, $u$- and $v$-fields in the $x$- and $y$-directions, respectively, for the three architectures. (It should be noted that the *displacement data are available as rectangular arrays over the ROI and at the center of each sub-image although they are displayed as contours* in these figures after post processing.).

In Figs. 12–14, one pair of displacement contours along with this respective speckle images, in the before and after crack initiation phases is presented. Away from the crack tip region, the deformations are consistent with the ones for flexural loading. As expected, the displacement fields near the crack tip vicinity are symmetric (mode-I) in the A1 architecture before and after crack initiation whereas they show noticeable asymmetry and mixed-mode (mode-I and -II) characteristics once the crack initiates in the A2 and A3 architectures. The crack tip was identified using crack opening displacement contours and the respective speckle images (Fig. 12–14). Then, as discussed earlier, the experimentally measured displacement field data from DIC for every image was imported into the respective FE mesh as two orthogonal boundary conditions at the corresponding nodes to compute the strain and stress fields. Subsequently, the fracture parameters namely the $J$-integral, $K_I$, and $K_{II}$ were all outputted by ABAQUS.

Fig. 15 shows the crack growth resistance or $J$-$a$ plots for all the three architectures. It can be observed from the graphs that the resistance to crack initiation, as expected, was the lowest for the A1 architecture (1850 J/m$^2$) and the same was approx. 55 % higher for A2

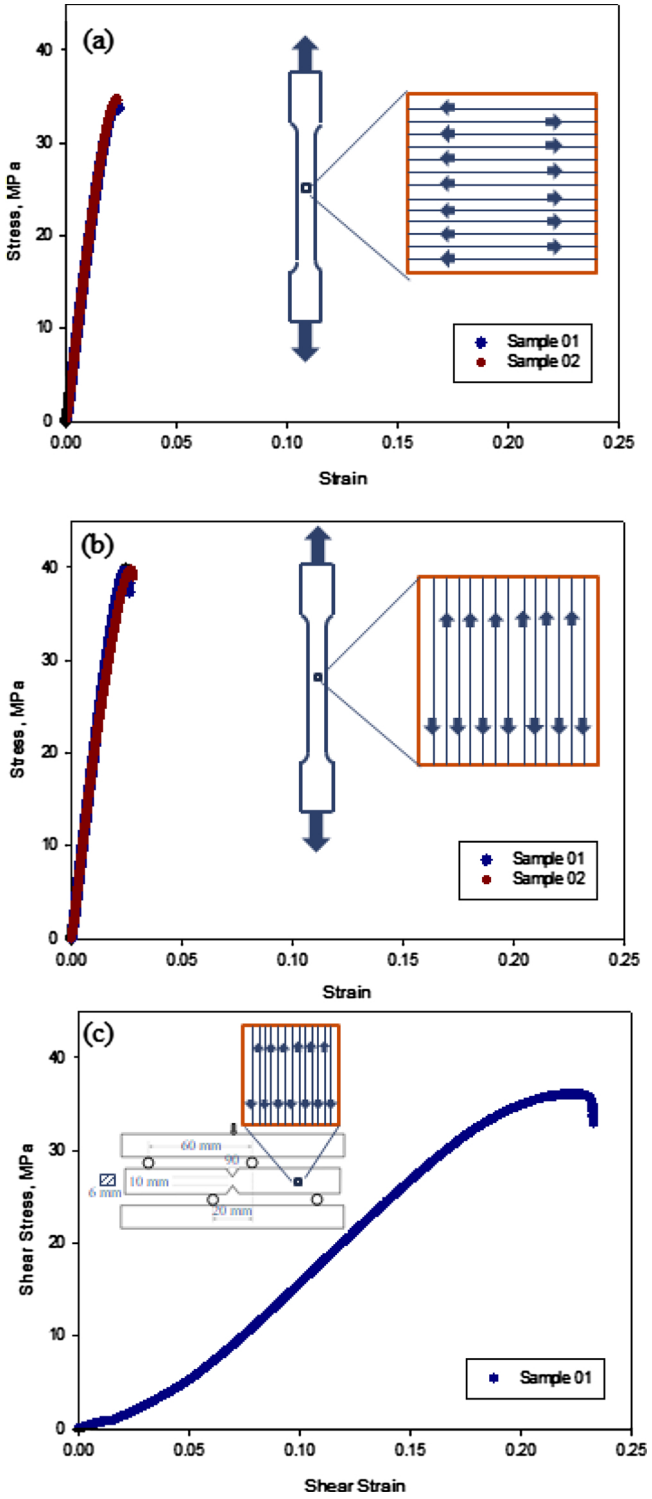


**Fig. 9.** Tensile and shear responses of unidirectionally printed reference coupons. **(a)** Stress-strain plots for unidirectional $[0^\circ]_n$ tensile samples with print architecture. **(b)** Stress-strain plots for unidirectional $[90^\circ]_n$ tensile samples with print architecture. **(c)** Shear stress- shear strain plots for $[0^\circ]_n$ Iosipescu tests with specimen geometry, loading and print architecture.

(2900 J/m$^2$) and 35 % higher for A3 (2500 J/m$^2$) architectures. After crack initiation, the crack growth resistance for the A1 architecture remained approx. constant or $dJ/da \sim 0$ whereas the A2 architecture showed an abrupt drop in resistance ($dJ/da < 0$ or unstable growth relative to its value at initiation) after crack initiation before building back resistance and attain $dJ/da > 0$. The A3 architecture, unlike the A2 counterpart, after crack initiation showed a steady increase in values or $dJ/da > 0$ before plateauing at ~4000 J/m$^2$, higher than that for A2 over the same amount of crack growth. The maximum values of the *J*-integral for each of these architectures in the window of observation were approx. 2250, 4000, 4450 J/m$^2$ for A1, A2, and A3, respectively.

**Table 3**
Material properties of reference architectures.

| Material Property | $[0^\circ]_n$ | $[90^\circ]_n$ | Iosipescu Shear |
|---|---|---|---|
| Elastic/Shear modulus (GPa) | 2.10 | 2.15 | 0.8 |
| Poisson's ratio | 0.34 | 0.34 | 0.34 |
| Failure stress (MPa) | 34.8 | 39.8 | 36.1 |
| Failure strain % | 2.2 | 2.4 | 22.2 |

Fig. 16 shows the *J*-integral histories from the 3-point bend specimens. For the purpose of comparing the fracture behaviors, *the time axes for each case are shifted such that t = 0 corresponds to crack initiation*. That is, the negative and positive *t* values correspond to pre- and post-initiation regimes, respectively.[3] Observations and characteristics similar to the ones made for the resistance behaviors (Fig. 15) can be made again. The architecture A1 had a brittle response whereas A2 and A3 were relatively tougher. Again, the A2 architecture showed a noticeable drop in the *J*-integral immediately after crack initiation whereas A3 had a steady increase with respect to time.

As noted earlier, the *J*-integral computed from the proposed hybrid method was partitioned into mode-I and -II SIF histories under small scale yielding assumptions. The assumption was first verified by evaluating the SIFs using the load vs. load-point plots (Fig. 10(a)) in the closed form solution for 3-point bend specimen configuration:

$$K_I = \frac{FS}{BW^{3/2}} \frac{3\alpha^{1/2}[1.99 - \alpha(1-\alpha)\{2.15 - 3.93\alpha + 2.7\alpha^2\}]}{2(1+2\alpha)(1-\alpha)^{3/2}}, \alpha = \frac{a}{W} \quad (4)$$

where *F*, *S*, *W*, *B* and *a* denote applied load, beam span, height, thickness and crack length, respectively. This is shown for A1, A2 and A3 architectures in Fig. 16 where the solid symbols are the ones obtained from the DIC-FE analyses and the open symbols are from Eq. 4. Good agreement between the two is evident in each case (error percentages for A1, A2 and A3 at crack initiation are ~3.1 %, ~6.2 % and ~7.3 % respectively). The comparison for A2 and A3 is limited up to crack initiation since the closed form solution is invalid after crack initiation when it kinks away from its initial path whereas it is valid for the self-similar crack growth case of A1. This agreement can be further confirmed by the dominant strain, $\varepsilon_{yy}$, field for the three architectures (Fig. 17). Given the strain component corresponding to the peak stress for these materials is ~2%, strains of that magnitude are highly localized to the crack tip region < 2.5 mm radius beyond which the values drop-off rapidly and facilitate a successful adaptation of small scale yielding when computing individual SIF values.

Fig. 18 shows individual SIF histories for all the three architectures under quasi-static loading conditions. Again, the negative and positive *t* values correspond to pre- and post-initiation regimes, respectively. As in the load vs load-point displacements plots (Fig. 10(a)), A2 and A3 architectures had higher crack initiation SIF (or, crack initiation toughness) relative to the A1 counterpart.

All the three architectures had a monotonic increase in the effective SIF ($=\sqrt{K_I^2 + K_{II}^2}$) until crack initiation (not shown here for brevity). In terms of the mode-I SIF, $K_I$, the A2 architecture had the highest crack initiation toughness of ~2.4 MPa√m followed by ~2.2 MPa√m for the A3 and ~1.9 MPa√m for the A1 architecture. In case of A1, after crack initiation, $K_I$ values remained constant. The A2 architecture, on the other hand, showed a rapid and significant drop in the $K_I$ values after

[3] The repeatability of *J* vs. *t* was also ensured across multiple samples and architectures. Two such examples are shown in Appendix A, Fig. A3(b).

**Table 4**
Ultrasonically measured wave speeds, density, and elastic constants for the three different print architectures in three orthogonal directions. (Density of bulk ABS based on manufacturer supplied wire stock was ~1035 Kg/m$^3$ and hence porosity based on weight difference was ~1.18 %).

| Print Architecture | Axis of Measurement | Longitudinal Velocity $C_L$ (m/s) | Shear Velocity $C_S$ (m/s) | Density ρ (Kg/m$^3$) | Poisson's Ratio $\nu$ | Elastic Modulus $E$ (GPa) |
|---|---|---|---|---|---|---|
| A1 | $x$ | 2045 | 987 | 1022 | 0.348 | 2.66 |
| A1 | $y$ | 2041 | 986 | | 0.348 | 2.65 |
| A1 | $z$ | 2035 | 983 | | 0.348 | 2.63 |
| A2 | $x$ | 2041 | 984 | 1022 | 0.349 | 2.67 |
| A2 | $y$ | 2038 | 986 | | 0.347 | 2.67 |
| A2 | $z$ | 2061 | 988 | | 0.351 | 2.69 |
| A3 | $x$ | 2060 | 988 | 1022 | 0.348 | 2.67 |
| A3 | $y$ | 2058 | 987 | | 0.347 | 2.68 |
| A3 | $z$ | 2061 | 985 | | 0.349 | 2.68 |

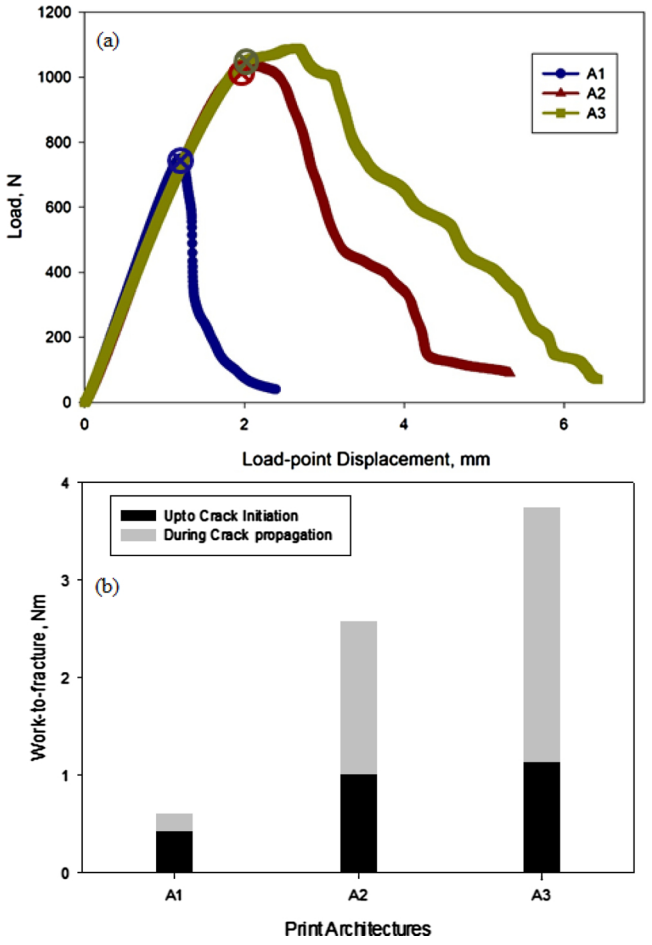


**Fig. 10. (a).** Effect of print architecture on load vs load-point deflection for quasi-static three-point bend specimens. **(b).** Work done on each print architecture before and after crack initiation in quasi-static experiments up to load drop to 200 N.

crack initiation followed by somewhat steady state values, well below that for A1, in the observation window. The mode-II SIF, $K_{II}$, on the other hand, after crack initiation showed a rapid rise followed by a steady state where the values reached the one at crack initiation. In the A3 architecture, after crack initiation, a gradual drop in $K_I$ was observed followed by a steady state region, below that for A1 but significantly higher than that for A2, for the rest of the window of observation. The $K_{II}$ values again had a rapid increase after crack initiation which eventually reached a steady state more gradually when compared to that for A2. These suggest that a relatively desirable failure of the A3 architecture relative to the other two although the crack initiation occurred at a slightly lower mode-I SIF when compared to the A2 counterpart.

## 5. Discussion

As evident from the above description of results for the three print architectures A1, A2, and A3, the tension tests and fracture tests show a few unexpected behaviors. The elastic properties of all three print architectures measured using quasi-static tension tests on dog-bone specimens or using ultrasonic measurements, showed nominally identical values suggesting elastic isotropy at the macroscale. As to be expected, the ultrasonic measurements yielded higher elastic moduli (2.6–2.7 GPa) when compared to the quasi-static counterparts (2.05–2.15 GPa). The tension tests revealed that the print architectures affect the ultimate stress only marginally; the A1 architecture was found to be the weakest relative to the other two. The print architecture, however, influenced ductility the most. The strain at failure measurements showed substantial differences; ~2.5 % for A1, ~9% for A2 and unexpectedly higher value of ~11 % for A3.

The quasi-static crack initiation toughness (or the critical SIF) values for A1 and A2 were the lowest (~2.0 MPa√m) and the highest (~2.5 MPa√m), respectively, with an intermediate value for A3 (~2.3 MPa√m). In the quasi-static case, although A2 showed the highest critical SIF, A3 produced a graceful or a gradual failure behavior ($dJ/da > 0$) with higher resistance to crack growth in terms of the measured $J$-integral.

Some insight into unexpectedly higher ductility of A3 relative to A2 and A1 could be gained from uniaxial tension tests on different unidirectional reference architectures. The results are shown in Fig. 9. Fig. 9(a) and (b) shows the tensile stress-strain responses. The results (peak stress ~35 MPa for 0° print and ~40 MPa for the 90° print, strain-at-failure ~2.4 % in both cases) are nearly same as the one for the A1 (Fig. 7) architecture. The pure shear tests (Fig. 9(c)), on the other hand, show that the ultimate shear stress is ~35 MPa, close to the tensile strength of the unidirectional coupons. However, the shear strain at failure is ~23 %, ten times higher than the tensile failure strain of the 0° or 90° print (and the A1 architecture). This suggests that ductility of a printed architecture can be influenced favorably by forcing the failure to occur in shear instead of tension.

Despite these results, the fact that ductility of A3 is greater than that for A2 suggests additional mechanisms at play. The synergistic constraint effects of different print directions are likely contributors in this regard. For example, Jhaver and Tippur [41] observed an increased plateau stress during compression of a hybrid co-continuous (interpenetrating) foam material made of closed-cell polymer foam infiltrated into an aluminum open-cell foam scaffold. Their hybrid foam showed ~50 % higher plateau stress and 35 % higher energy absorption per unit mass relative to the syntactic foam and it was attributed to synergistic constraint effects. The $[0/45/90/-45°]_n$ layering in A3 architecture is expected to perform a similar function. That is, the 90° print

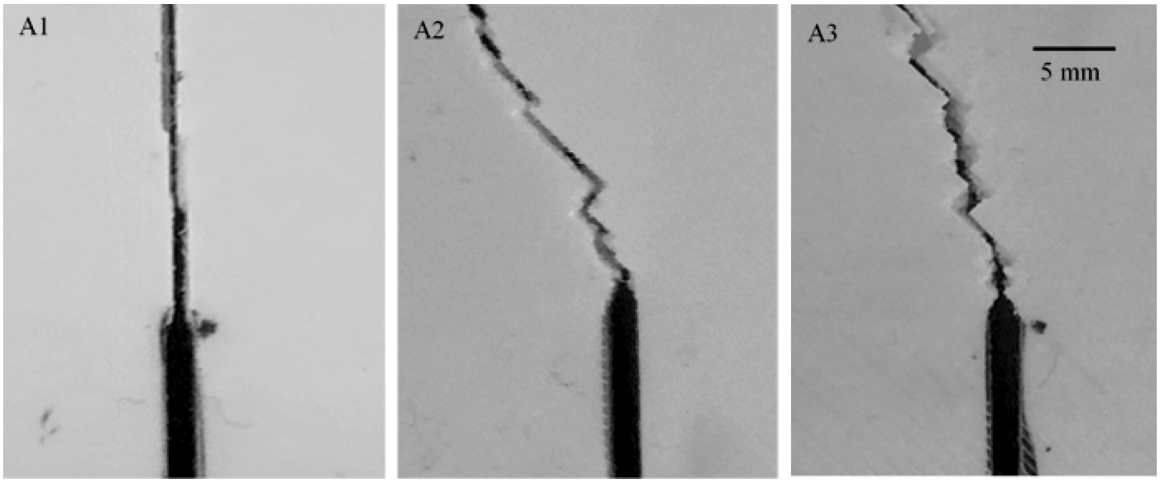


**Fig. 11.** Photographs of observed crack paths in fractured 3-point bend specimens. (The specimen A3 is flipped by 180° for consistency with A2).

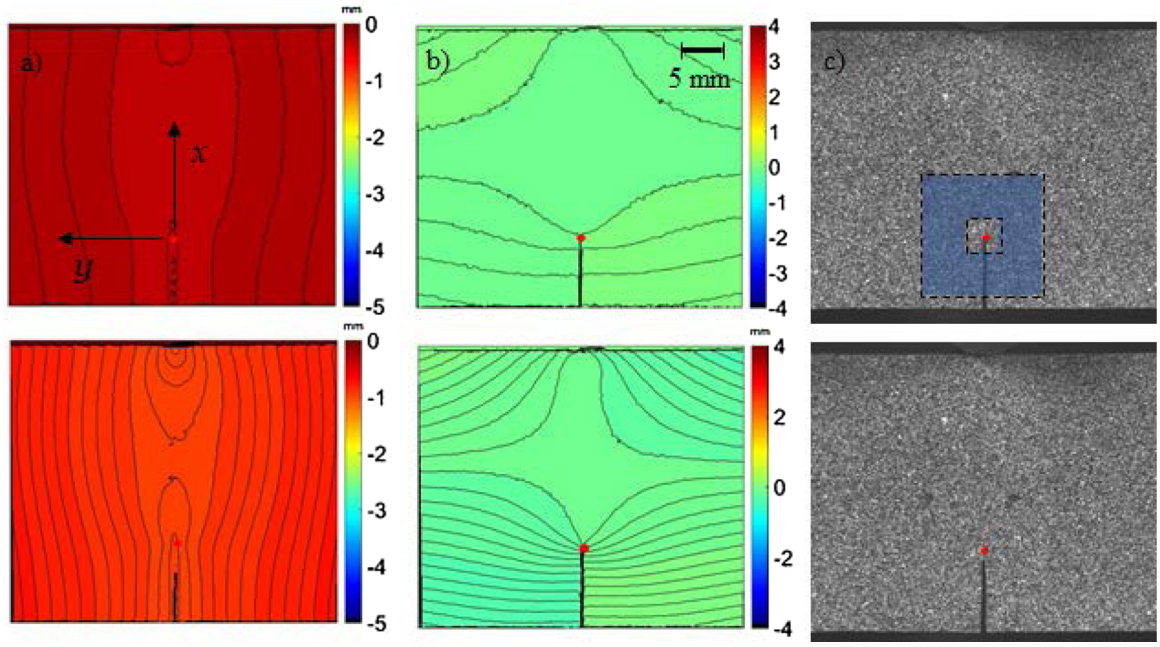


**Fig. 12.** Displacement contours of A1, with a contour interval of 20 μm, obtained through DIC **(a)** *x*- or *u*-field, **(b)** *y*-or *v*-field. **(c)** Speckle images corresponding to the applied load step. Red solid dots indicate the crack tip location at this time/load step. Top row corresponds to pre-crack initiation (Load = 500 N) and bottom row corresponds to post-crack initiation (Load step = 620 N) stages. (The shaded zone in the speckle image corresponds to the region where the *J*-integral is computed.). (For interpretation of the references to colour in this figure legend, the reader is referred to the web version of this article).

layer mitigates the tensile stress on the 45° and -45° layers accommodating higher shear deformations to occur.

The tensile tests can also shed light on the observed fracture characteristics of the three architectures. The low crack initiation toughness followed by growth at a stable *J*-integral value for A1 is consistent with the low ductility observed in $[0^\circ]_n$ and $[90^\circ]_n$ coupons (Fig. 9). Relatively high crack initiation toughness followed by unstable crack growth along one of the two 45° directions in A2 is also consistent with the higher shear strain at failure in the Iosipescu sample as the crack kinks into a 45° plane and endures combined tensile and shear deformations. The back and forth switching between +45° and -45° planes also suggests the possibility of a jagged, instead of a straight, crack front and hence smeared deformations relative to A1. These failure mechanisms are further amplified in the A3 architecture with the crack front having opportunities for ± 45° as well as 0° growth along the weaker planes between the individual printed beads/strings and a macroscale growth in a direction not necessarily along ± 45°.

## 6. Conclusions

The tensile and fracture behaviors of additively manufactured ABS coupons are studied in order to understand the role print architectures have on mechanical performance of 3D printed parts. Specifically, three print architectures, A1 or $[0^\circ/90^\circ]_n$, A2 or $[45^\circ/\text{-}45^\circ]_n$ and A3 or $[0^\circ/45^\circ/90^\circ/\text{-}45^\circ]_n$, are studied. The optical method of 2D-DIC is found suitable for mapping crack tip deformations in 3D printed specimens in the whole field before crack initiation and during crack growth. A method of transferring optically measured displacement fields to companion finite element models as surface boundary conditions over the whole field for extracting failure parameters using in-built domain integral algorithm for *J*-integral evaluation is also presented. Subsequently, individual SIFs are evaluated by computing the interaction integral and mode-partitioning method using auxiliary fields.

The tensile test results show that the printed parts of all three architectures are macroscopically isotropic in terms of their elastic

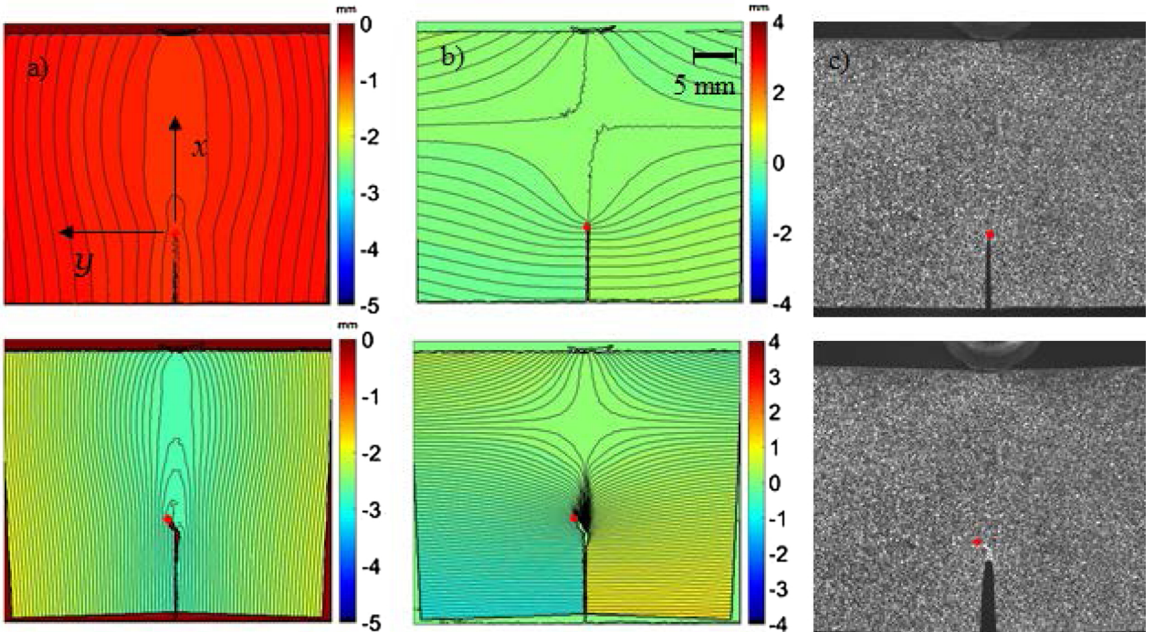


**Fig. 13.** Displacement contours of A2, with contour interval of 20 μm, obtained through DIC **(a)** *x*- or *u*-field, **(b)** *y*-or *v*-field. **(c)** Speckle images corresponding to the load step. Red solid dots indicate the crack tip at this time step. Top row corresponds to pre-crack initiation (Load = 530 N) and bottom row corresponds to post-crack initiation (Load = 890 N) stages. (For interpretation of the references to colour in this figure legend, the reader is referred to the web version of this article).

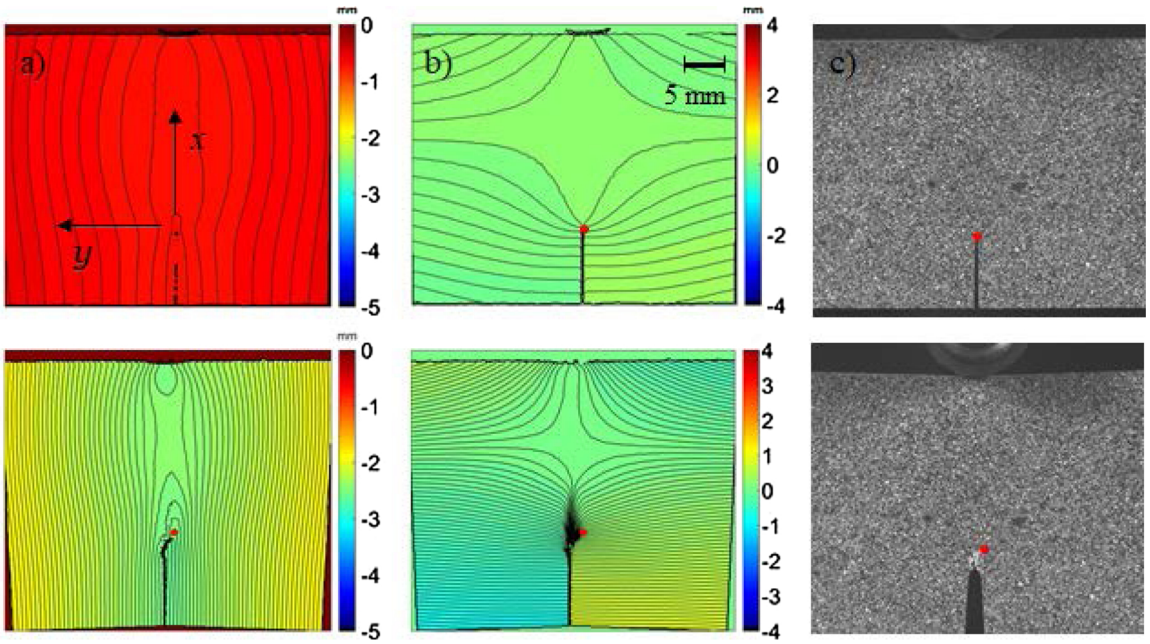


**Fig. 14.** Displacement contours of A3, with contour interval of 20 μm, obtained through DIC **(a)** *x*- or *u*-field, **(b)** *y*-or *v*-field. **(c)** Speckle images corresponding to the load step. Red solid dots indicate the current crack tip at each time/load step. Top row corresponds to pre-crack initiation (Load = 510 N) and bottom row corresponds to post-crack initiation (Load step = 991 N) stages. (For interpretation of the references to colour in this figure legend, the reader is referred to the web version of this article).

properties within experimental errors. A follow up ultrasonic evaluation further confirms this elastic isotropy. However, distinctly different failure stresses, failure strains, and fracture surface morphologies are observed in these three print architectures during tension tests. The ductility and toughness are higher for the A2 and A3 architectures when compared to that of A1 counterpart. The higher failure strain is attributable to shear deformations evident from the failed specimen cross-section. The A3 architecture shows surprisingly higher ductility relative to A2 and synergistic constraint effects among different layers contributes to such an enhancement. This in turn raises the possibility of tailoring macroscale mechanical behavior by microscale manipulation of print architectures via 3D printing of parts.

The fracture results show that the fracture toughness of A2 and A3 architectures are higher than the A1 counterpart. The results also indicate that higher ductility and energy absorption occur during crack growth for these two architectures but different failures modes and crack propagation paths are observed. The architecture A2 is found to have the highest crack initiation toughness whereas architecture A3 offers higher crack growth resistance with a marginally lower crack initiation toughness. The crack growth occurs in A2 along

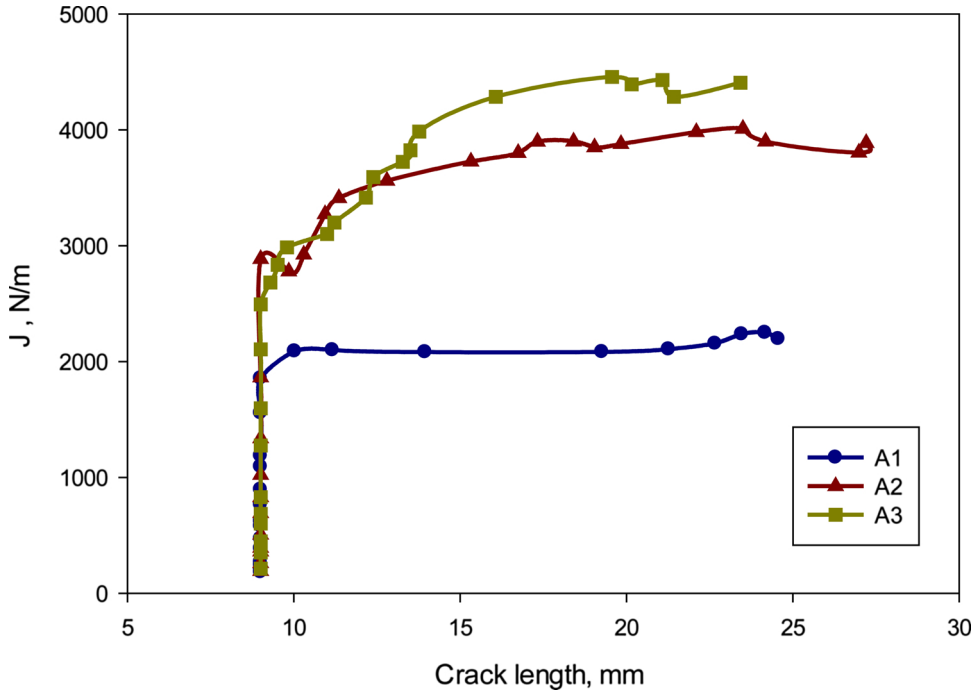


**Fig. 15.** Crack growth resistance curves for 3-point bend specimens under static condition.

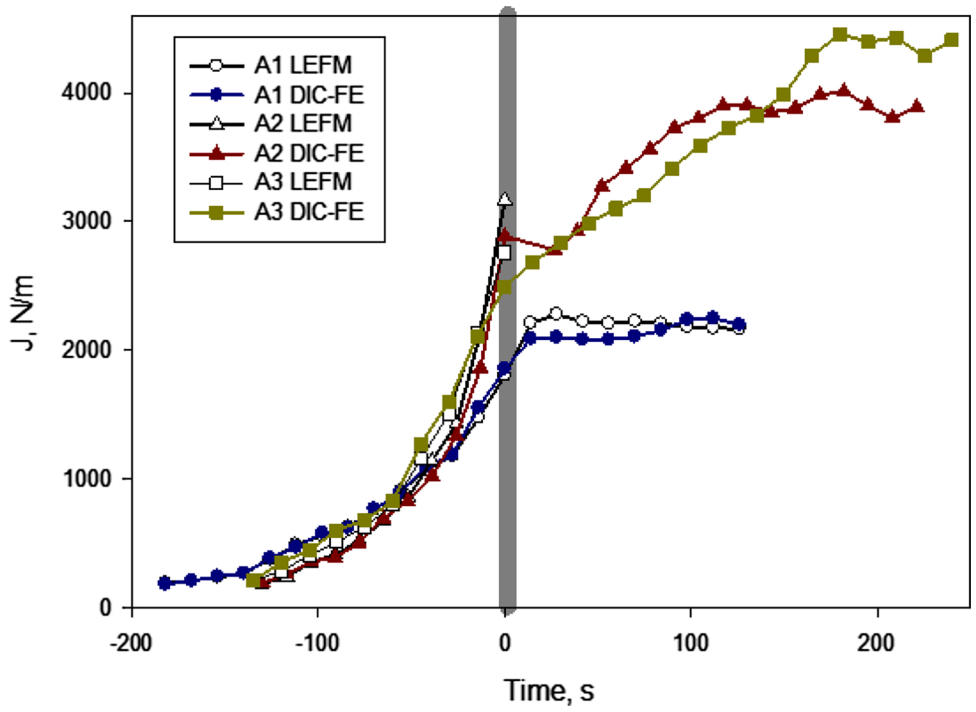


**Fig. 16.** The *J*-Integral histories for 3-point bend specimens under static conditions. Comparison between the proposed DIC-FE approach and closed form solution based on small scale yielding for A1, A2 and A3 architectures. (Negative and positive times correspond to pre- and post-crack initiation regimes.).

nominally ± 45° planes in a staircase pattern whereas the same is much more tortuous in A3 due to crack growth along ± 45° as well as 0° planes. The mechanics of these distinctly different failure behaviors are explained in terms of tension and shear tests on unidirectional (reference) tensile and shear specimens. The high ductility observed during pure shear tests explains the failure behaviors seen in the fracture specimens.

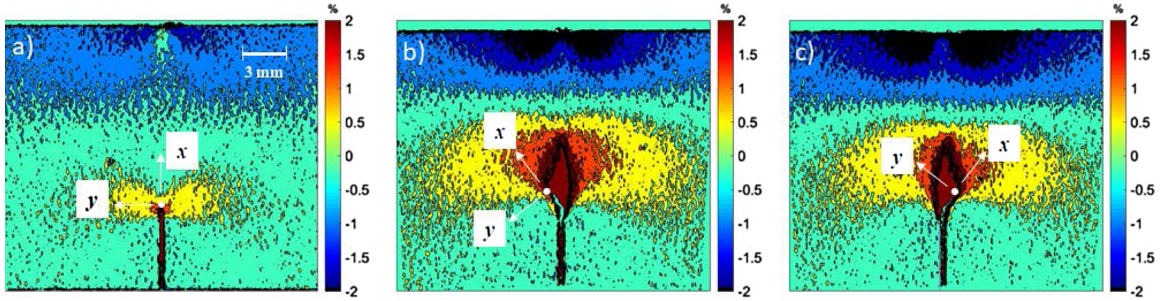


**Fig. 17.** Dominant $\varepsilon_{yy}$ strain fields for (a) A1 (Load = 661 N), (b) A2 (Load = 710 N) and (c) A3 (Load = 740 N) architectures *during crack propagation*. Solid dots indicate the crack tip location at this time/load step.

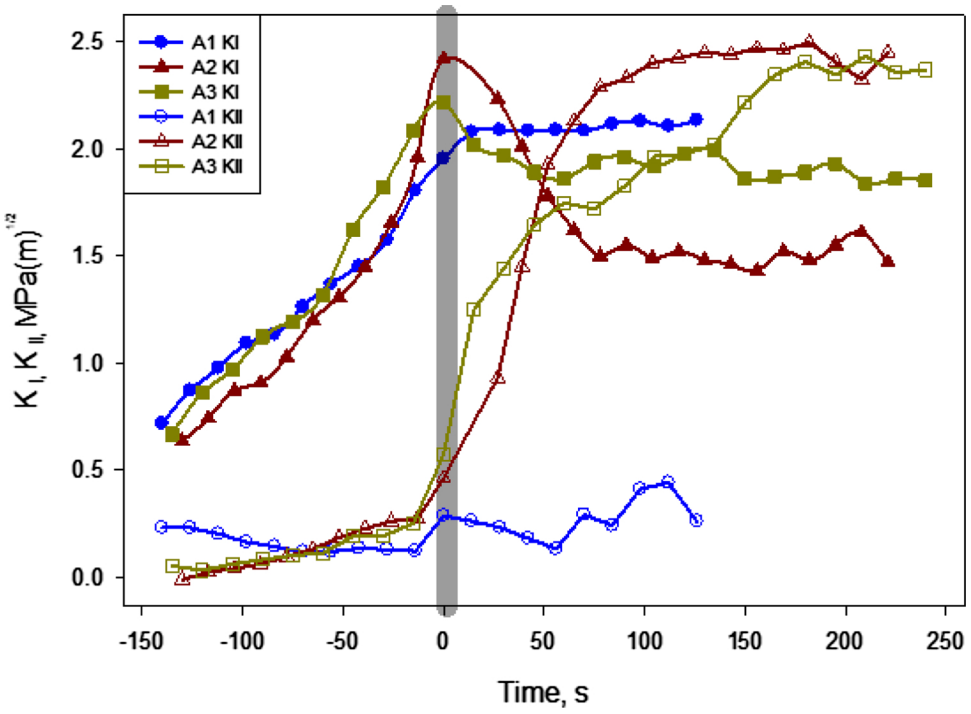


**Fig. 18.** SIF histories for 3-point bend specimens of A1, A2 and A3 architectures under quasi-static loading conditions. (Negative and positive times correspond to pre- and post-crack initiation regimes.).

## Author's statement

Authors acknowledge that this paper does not involve experimentation with human subjects.

## Declaration of Competing Interest

The authors reported no declarations of interest.

## Acknowledgements

The authors would like to acknowledge the support of 2018 PAIR Tier III grant, 'Creating better bio-medical implants for patients in need using additive manufacturing,' (PI: Dr. Nima Shamsaei) from Auburn University.

## Appendix A

A summary of the experimental parameters used for 2D DIC is listed in Table A1.

J-integral and SIF Error Estimation: The errors in the *J*-Integral and $K_I$ and $K_{II}$ values were also estimated based on the accuracy of locating the crack tip from the speckle images. Fig. A1 shows an example for the A2 architecture during mixed-mode crack propagation. In this, different crack tip locations were obtained by multiple identification attempts on the same speckle image. Five such crack tip locations are numbered 1-5. They correspond to sites [(991, 1306), (992, 1307), (994, 1308), (993, 1308), (993, 1309)] in the image in pixel coordinates. Evidently the crack tip was identifiable with ± 2 pixel variation. The resulting variation of the *J*-integral and SIFs for increasing number of contours are plotted. The error in *J* and SIF values after averaging the data in the plateau region for each was less than 2% showing the robustness of the approach.

Test Details and Experimental Repeatability: The spray-painted random speckles were recorded to measure longitudinal and lateral strains in the gage section of the specimen using DIC to enable evaluation of the elastic constants *E* and Poisson's ratio □ for each architecture. A pair of

**Table A1**
DIC parameters summary.

| Hardware Parameters | | Analysis Parameters | |
|---|---|---|---|
| Camera Manufacturer | Point Grey | Software Package Name | Aramis® 6.2.0 |
| Model | Grasshopper3 GS3-U3-41C6M | Manufacturer | GOM |
| Image Resolution | 2048 x 2048 | | |
| Lens Manufacturer | | | |
| Model | Computar Lens | Image Filtering | None |
| Focal Length | 18-108 mm | | |
| FOV | 60 mm x 60 mm | Sub-image/Subset Size | 25 x 25 |
| Image Scale | 33.3 pixel/mm | Step Size | 5 |
| Stereo-Angle | N/A | Subset Shape Function | Affine |
| Stand-Off Distance | 0.8 m | Data Processing and Filtering for QOIs | None |
| Image Acquisition Rate | 2 fps | Noise-floor and Bias of QOIs | 1 μm |
| Patterning Technique | Spray painted | | |
| Approx. Feature Size | 5 pixels | | |

representative displacement fields from the uniaxial test on A1 architecture is shown in Fig. A2(a). It also shows stress vs. longitudinal and lateral strain plots in the linear range for this architecture (Fig. A2(b)). Multiple tension and fracture samples of each of the architectures were tested in order to ensure repeatability. Some examples in this regard are shown in Fig. A3. Fig. A3(a) show two repeatable tension tests for all three architectures A1, A2 and A3. The extracted values of the *J*-integral for two A1 and two A2 samples over pre- and post-crack initiation phases are presented in Fig. A3(b). Again, in these experiments involving crack initiation and growth events, the *J*-integral histories were quite repeatable.

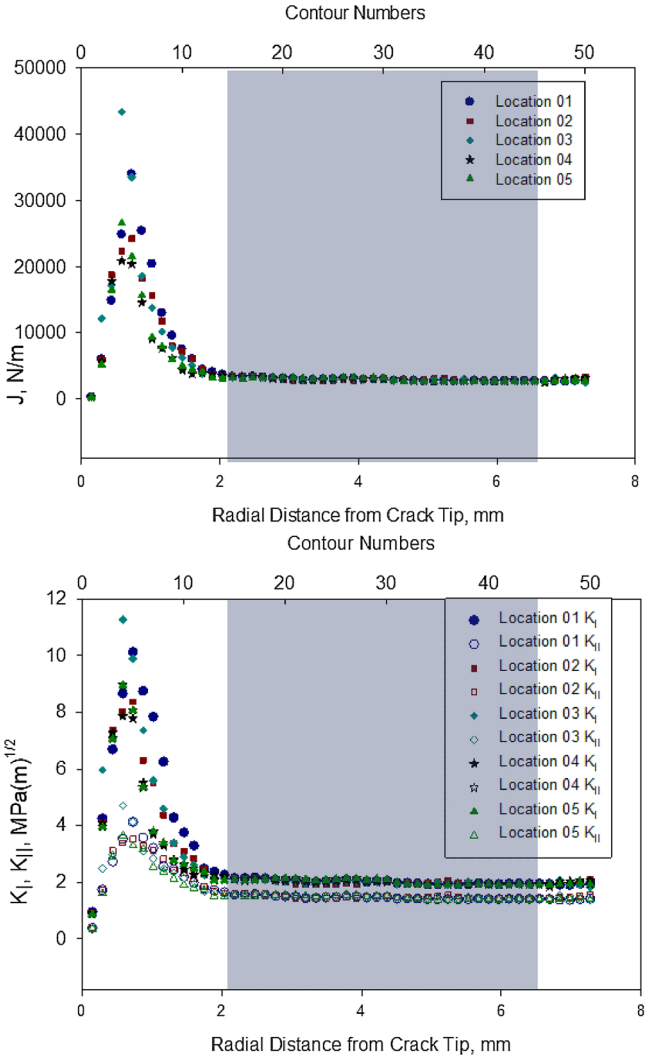


**Fig. A1.** Variation of computed *J*-value and SIFs for A2 architecture at an instant during crack growth. Each data set corresponds to five different crack tip locations due to identification error. Contour #15-45 corresponding to approx. 2.25-7 mm or *r*/*B* ratio of 0.4-1.2 was used to find the average. The *J*-value and SIFs varies by < 5% in the shaded part for each location and < 2% between different locations.

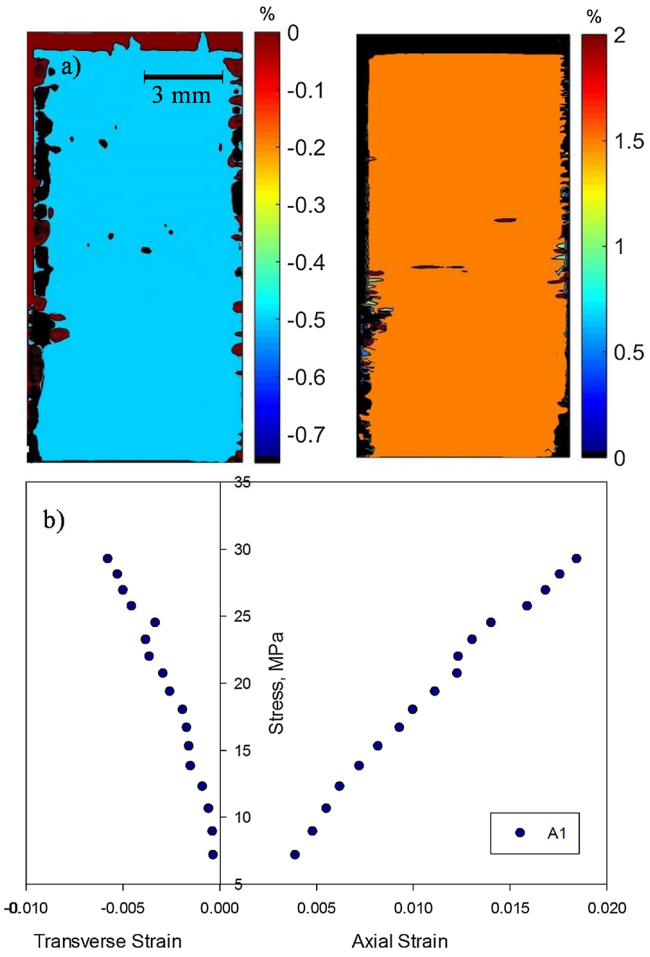


**Fig. A2.** Uniaxial tension test results from DIC: **(a)** $\varepsilon_{xx}$ and or $\varepsilon_{yy}$ strain fields of A1 architecture **(b)** Stress vs. axial and transverse strain plots of A1 architecture used to calculate elastic modulus and Poisson's ratio.

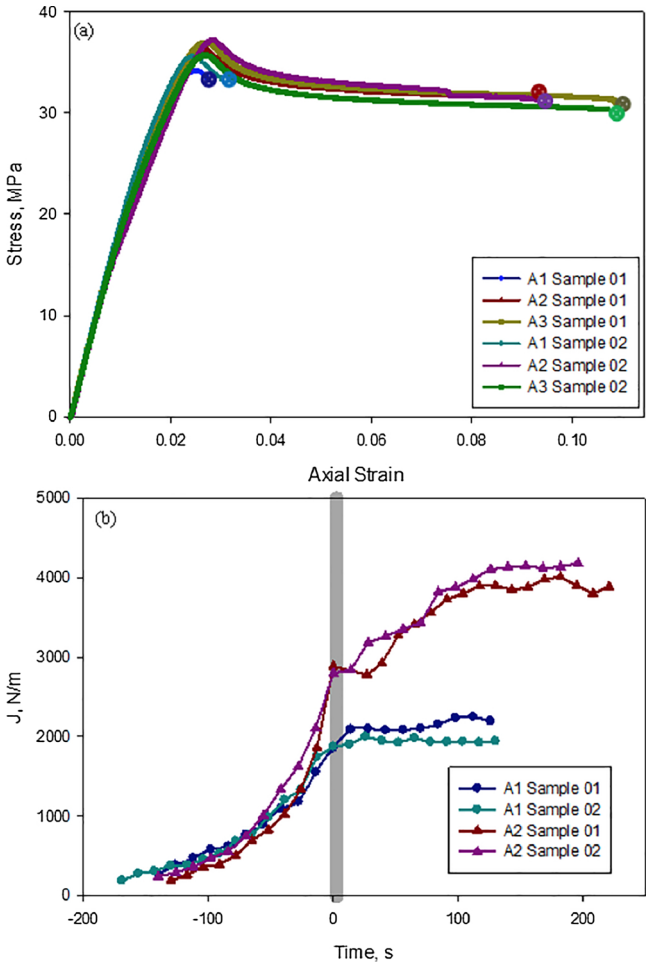


**Fig. A3. (a)** Repeatability for tensile stress-strain responses for all three architectures. **(b)** Repeatability for *J* vs. Time plots for the A1 and A2 architectures.

## References


[1] Standard Terminology for Additive Manufacturing Technologies, ASTM International Designation, 2012 F2792-12a.

[2] O. Mohamed, S. Masood, J. Bhowmik, Optimization of fused deposition modeling process parameters: a review of current research and future prospects, Adv. Manuf. 3 (1) (2015) 42–53.

[3] D. Bourell, D. Rosen, M. Leu, The roadmap for additive manufacturing and its impact, 3D Print. Addit. Manuf. 1 (1) (2014) 6–9.

[4] S. Ahn, M. Montero, D. Odell, S. Roundy, P. Wright, Anisotropic material properties of fused deposition modeling ABS, Rapid Prototyp. J. 8 (4) (2002) 248–257.

[5] A. Al-Maharma, P. Sendur, Review of the main factors controlling the fracture toughness and impact strength properties of natural composites, Mater. Res. Express 6 (2) (2018) 022001.

[6] J. Dizon, A. Espera, Q. Chen, R. Advincula, Mechanical characterization of 3D-printed polymers, Addit. Manuf. 20 (2018) 44–67.

[7] K. Van de Velde, P. Kiekens, Biopolymers: overview of several properties and consequences on their applications, Polym. Test. 21 (4) (2002) 433–442.

[8] P. Poh, M. Chhaya, F. Wunner, E.M. De-Juan-Pardo, et al., Polylactides in additive biomanufacturing, Adv. Drug Deliv. Rev. 107 (2016) 228–246.

[9] J.C. Riddick, M.A. Haile, R.V. Wahlde, D.P. Cole, O. Bamiduro, T.E. Johnson, Fractographic analysis of tensile failure of acrylonitrile-butadiene-styrene fabricated by fused deposition modeling, Addit. Manuf. 11 (2016) 49–59.

[10] H. Akiyama, M. Uchida, Y. Kaneko, Evaluation of effect of sample size and layer direction on mechanical property of specimen manufactured by FDM-Type 3D printer, Key Eng. Mater. 794 (2019) 324–332.

[11] J. Gardan, A. Makke, N. Recho, A method to improve the fracture toughness using 3D printing by extrusion deposition, Procedia Struct. Integr. 2 (2016) 144–151.

[12] P. Lanzillotti, J. Gardan, A. Makke, N. Recho, Enhancement of fracture toughness under mixed mode loading of ABS specimens produced by 3D printing, Rapid Prototyp. J. 25 (4) (2019) 679–689.

[13] E. Papon, A. Haque, Fracture toughness of additively manufactured carbon fiber reinforced composites, Addit. Manuf. 26 (2019) 41–52.

[14] Z. Jia, L. Wang, 3D printing of biomimetic composites with improved fracture toughness, Acta Mater. 173 (2019) 61–73.

[15] T.D. Mclouth, J.V. Severino, P.M. Adams, D.N. Patel, et al., The impact of print orientation and raster pattern on fracture toughness in additively manufactured ABS, Addit. Manuf. 18 (2017) 103–109.

[16] N. Aliheidari, R. Tripuraneni, A. Ameli, S. Nadimpalli, Fracture resistance measurement of fused deposition modeling 3D printed polymers, Polym. Test. 60 (2017) 94–101.

[17] A.N. Dickson, D.P. Dowling, Enhancing the bearing strength of woven carbon fibre thermoplastic composites through additive manufacturing, Compos. Struct. 212 (2019) 381–388.

[18] A.D. León, A. Domínguez-Calvo, S. Molina, Materials with enhanced adhesive properties based on acrylonitrile-butadiene-styrene (ABS)/thermoplastic polyurethane (TPU) blends for fused filament fabrication (FFF), Mater. Des. 182 (2019) 108044.

[19] D. Young, N. Wetmore, M. Czabaj, Interlayer fracture toughness of additively manufactured unreinforced and carbon-fiber-reinforced acrylonitrile butadiene styrene, Addit. Manuf. 22 (2018) 508–515.

[20] M. Rabbi, V. Chalivendra, D. Li, A novel approach to increase dynamic fracture toughness of additively manufactured polymer, Exp. Mech. 59 (6) (2019) 899–911.

[21] M. Samykano, S.K. Selvamani, K. Kadirgama, W.K. Ngui, et al., Mechanical property of FDM printed ABS: influence of printing parameters, Int. J. Adv. Manuf. Technol. 102 (9–12) (2019) 2779–2796.

[22] K.R. Hart, E.D. Wetzel, Fracture behavior of additively manufactured acrylonitrile butadiene styrene (ABS) materials, Eng. Fract. Mech. 177 (2017) 1–13.

[23] S.C. Ligon, R. Liska, J. Stampfl, M. Gurr, R. Mülhaupt, Polymers for 3D printing and customized additive manufacturing, Chem. Rev. 117 (15) (2017) 10212–10290.

[24] B. Pan, K. Qian, H. Xie, A. Asundi, Two-dimensional digital image correlation for in-plane displacement and strain measurement: a review, Meas. Sci. Technol. 20 (6) (2009) 062001.

[25] S. Yoneyama, T. Ogawa, Y. Kobayashi, Evaluating mixed-mode stress intensity factors from full-field displacement fields obtained by optical methods, Eng. Fract. Mech. 74 (9) (2007) 1399–1412.

[26] D. Lee, H.V. Tippur, M. Kirugulige, P. Bogert, Experimental study of dynamic crack growth in unidirectional graphite/epoxy composites using digital image correlation method and high-speed photography, J. Compos. Mater. 43 (9) (2009) 2081–2108.

[27] M.S. Kirugulige, H.V. Tippur, Measurement of fracture parameters for a mixed-mode crack driven by stress waves using image correlation technique and high-

speed digital photography, Strain 45 (2009) 108–122.
[28] S. Barhli, M. Mostafavi, A. Cinar, D. Hollis, et al., J-integral calculation by finite element processing of measured full-field surface displacements, Exp. Mech. 57 (6) (2017) 997–1009.
[29] R.M. Pitti, C. Badulescu, M. Grédiac, Characterization of a cracked specimen with full-field measurements: direct determination of the crack tip and energy release rate calculation, Int. J. Fract. 187 (1) (2014) 109–121.
[30] T.H. Becker, M. Mostafavi, R.B. Tait, T.J. Marrow, An approach to calculate the J-integral by digital image correlation displacement field measurement, Fatigue Fract. Eng. Mater. Struct. 35 (10) (2012) 971–984.
[31] T. Becker, T. Marrow, R. Tait, Damage, crack growth and fracture characteristics of nuclear grade graphite using the double torsion technique, J. Nucl. Mater. 414 (1) (2011) 32–43.
[32] T. Hareesh, F. Chiang, Integrated experimental-finite element approach for studying elasto-plastic crack-tip fields, Eng. Fract. Mech. 31 (3) (1988) 451–461, https://doi.org/10.1016/0013-7944(88)90087-2.
[33] N.P. O'Dowd, C.F. Shih, M.G. Stout, Test geometries for measuring interfacial fracture toughness, Int. J. Solids Struct. 29 (5) (1992) 571–589.
[34] M.S. Kirugulige, H.V. Tippur, T.S. Denney, Measurement of transient deformations using digital image correlation method and high-speed photography: application to dynamic fracture, Appl. Opt. 46 (22) (2007) 5083.
[35] G. Cherepanov, Crack propagation in continuous media, J. Appl. Math. Mech. 31 (3) (1967) 503–512.
[36] J.R. Rice, A path independent integral and the approximate analysis of strain concentration by notches and cracks, J. Appl. Mech. 35 (2) (1968) 379–386.
[37] K. Jajam, H. Tippur, An experimental investigation of dynamic crack growth past a stiff inclusion, Eng. Fract. Mech. 78 (6) (2011) 1289–1305.
[38] R.W. Bedsole, P.B. Bogert, H.V. Tippur, An experimental investigation of inter-laminar and intralaminar dynamic fracture of CFRPs: effect of matrix modification using carbon nanotubes, Compos. Struct. 132 (2015) 1043–1055.
[39] L. Xu, H.V. Tippur, Fracture parameters for interfacial cracks: an experimental-finite element study of crack tip fields and crack initiation toughness, Int. J. Fract. 71 (4) (1995) 345–363.
[40] C.F. Shih, R.J. Asaro, Elastic-plastic analysis of cracks on bimaterial interfaces: part I—small scale yielding, J. Appl. Mech. (1988) 299–316.
[41] R. Jhaver, H. Tippur, Processing, compression response and finite element modeling of syntactic foam based interpenetrating phase composite (IPC), Mater. Sci. Eng. A 499 (1–2) (2009) 507–517.